BRAIN
ORIGINAL ARTICLE

Early glymphatic failure in *App*$^{NL-F}$ knock-in mice is linked to parenchymal border macrophages loss

Na Liu,[1,2] Yiyi Yang,[1] Marios Kritsilis,[1,2] Kelley M. Swanberg,[1,2] Chenchen Liu,[1,2,3] Xuanhui Liu,[1,2] Brecht Moonen,[1,2,4] Tomas Deierborg,[1] Per Nilsson,[5] Stina Syvänen,[6] Dag Sehlin[6] and Iben Lundgaard[1,2]

See Bhardwaj and Benveniste (https://doi.org/10.1093/brain/awag197) for a scientific commentary on this article.

Amyloid-β (Aβ) accumulation is a hallmark of Alzheimer's disease. Cerebral Aβ deposition is attenuated by a functional glymphatic system, in which perivascular entry of CSF and its exchange with interstitial fluid mediate solute clearance. Parenchymal border macrophages (PBMs), positioned along glymphatic pathways, are emerging as important players for glymphatic clearance. However, how glymphatic function and PBMs are affected in *App* knock-in models of Alzheimer's disease is unknown.

In this study, we used two *App* knock-in mouse models that develop progressive Aβ pathology, *App*$^{NL-F}$ and *App*$^{NL-G-F}$. *App*$^{NL-F}$ mice showed reductions in glymphatic influx and clearance at 6 months, preceding substantial Aβ plaque deposition. The decrease in glymphatic function in *App*$^{NL-F}$ mice was correlated with a loss of PBMs and altered marker expression. Acute administration of Aβ into the CSF decreased the number of PBMs and impaired glymphatic transport in wild-type mice, thus recapitulating the pre-plaque stage. In contrast, the number of PBMs was not reduced in *App*$^{NL-G-F}$ mice, possibly owing to an enhanced Aβ phagocytic capacity in PBMs. Four weeks of systemic anti-Aβ antibody treatment efficiently reduced Aβ plaque load and rescued PBMs in some brain regions; however, the treatment did not restore glymphatic function in the *App*$^{NL-F}$ model.

These findings suggest that glymphatic dysfunction in *App* knock-in models of Alzheimer's disease is not driven by parenchymal Aβ plaque load but is closely linked to pre-plaque Aβ-induced loss of PBMs. Preservation of PBM abundance and their normal marker expression might be important for maintaining glymphatic function and mitigating early progression of Alzheimer's disease.

1 Department of Experimental Medical Science, Lund University, Lund 22184, Sweden
2 Wallenberg Centre for Molecular Medicine, Lund University, Lund 22184, Sweden
3 Department of Neurology, Tongji Hospital, Tongji Medical College, Huazhong University of Science and Technology, Wuhan 430030, China
4 Department of Immunology and Infection, Biomedical Research Institute, Hasselt University, Diepenbeek 3590, Belgium
5 Division of Neurogeriatrics, Center for Alzheimer Research, Department of Neurobiology, Care Sciences and Society, Karolinska Institutet, Stockholm 17177, Sweden
6 Department of Public Health and Caring Sciences, Uppsala University, Uppsala 75185, Sweden

Correspondence to: Iben Lundgaard
Department of Experimental Medical Science
Lund University, BMC A1304, Sölvegatan 19, Lund 22184, Sweden
E-mail: iben.lundgaard@med.lu.se

Received July 28, 2025. Revised January 07, 2026. Accepted January 30, 2026. Advance access publication February 28, 2026

Keywords: *App* knock-in Alzheimer's mice; glymphatic system; parenchymal border macrophages

Introduction

Alzheimer's disease is a leading cause of cognitive impairment and dementia worldwide, affecting ~5% of individuals aged 65–74 years and ≤33% of those aged ≥85 years.[1-3] One of its key histopathological hallmarks is the accumulation of amyloid-β (Aβ) plaques in the brain.[4]

Emerging evidence suggests that the glymphatic system contributes to clearing protein waste, including Aβ peptide, through a network of perivascular channels.[5-8] This fluid transport is critically dependent on aquaporin-4 (AQP4) water channels polarized to the vascular endfeet of astrocytes.[9-11] In humans, loss of perivascular AQP4 localization is correlated with increased Aβ burden,[12,13] and experimental disruption of glymphatic function in rodents accelerates Aβ deposition.[14-16] Although these findings demonstrate that glymphatic impairment can worsen Aβ pathology, potential changes in the glymphatic system across the natural course of Alzheimer's disease remain incompletely understood, with existing animal studies reporting inconsistent outcomes.[17-19] Previous studies using transgenic amyloid precursor protein (APP) mouse models have demonstrated impaired glymphatic function in Alzheimer's disease.[15,17,20] However, concerns have been raised regarding potential artefacts resulting from the overexpression of APP-derived non-Aβ fragments in those models.[21,22] Therefore, preclinical studies using next-generation Alzheimer's disease models with greater physiological relevance, such as *App* knock-in models, are warranted.

Given the crucial role of AQP4 in facilitating glymphatic transport, its dysfunction has been proposed as a potential contributor to impaired glymphatic function in Alzheimer's disease.[17,23] However, a recent study showed that restoring perivascular AQP4 localization through adeno-associated virus (AAV)-mediated overexpression of AQP4-M23 at perivascular endfeet in Alzheimer's mice was insufficient to restore glymphatic flow or reduce brain Aβ deposition.[13] This suggests that additional regulatory mechanisms beyond AQP4 contribute to glymphatic impairment in Alzheimer's disease. Brain border-associated macrophages are specialized immune cells located at the interfaces of the brain, including the meninges, choroid plexus and perivascular spaces.[24] Among these, perivascular macrophages (PVMs) and leptomeningeal macrophages [collectively referred to as parenchymal border macrophages (PBMs)] reside along key anatomical routes of the glymphatic system and have recently been identified as key regulators of glymphatic flow.[14] PBMs have been shown to regulate glymphatic flow by influencing vascular pulsatility,[14] which is recognized as a crucial driving force of the glymphatic system.[25-27] As professional phagocytes,[24] PBMs perform immune surveillance at the brain borders and respond to both exogenous and endogenous antigens. Aβ pathology, especially soluble Aβ in the CSF, could be an important environmental stimulus for PBMs, because these cells reside at the brain borders and are directly exposed to the CSF. How such Aβ-driven changes shape PBM responses during Alzheimer's disease progression, and how these alterations might subsequently affect glymphatic transport, remain incompletely understood.

In this study, we investigated changes in glymphatic function during the progression of Alzheimer's disease and examined the contribution of PBMs to these alterations using physiologically relevant *App* knock-in mouse models. By integrating measurements of glymphatic transport with analyses of PBM alterations and Aβ pathology, we aimed to gain a better understanding of how PBM-related changes influence the glymphatic system in Alzheimer's disease.

Materials and methods

Animals

Male and female homozygous App^{NL-F} and App^{NL-G-F} knock-in mice were bred locally at Lund University and maintained on a C57BL/6 background. App^{NL-F} knock-in mice carry two familial Alzheimer's disease-associated mutations in the *App* gene: the Swedish mutation (NL) and the Iberian mutation (F), whereas App^{NL-G-F} knock-in mice additionally harbour the Arctic mutation (G).[22] Wild-type C57BL/6 mice (used as controls; WT) were purchased from Charles River Laboratories and Janvier Labs. Both male and female mice were used in experiments involving *App* knock-in mice: circular points denote female mice, and triangular points denote male mice in the graphs. Only male mice were used in the acute Aβ injection and clodronate-induced macrophage depletion experiments. Animals were housed in a climate-controlled facility under a standard 12 h–12 h light–dark cycle, in groups of two to five in individually ventilated cages with environmental enrichment and *ad libitum* access to normal food and water. All experiments were performed following international guidelines on experimental animal research and were approved by the Malmö-Lund Ethical Committee on Animal Research in Sweden (5.8.18-08269/2019, 5.8.18-20240/2021, V 2023/1245 and 5.8.18-04510/2024). Animals were allocated randomly to experimental groups where applicable.

Cisterna magna injection

Mice were anaesthetized with an intraperitoneal injection of ketamine (100 mg/kg) and xylazine (20 mg/kg). After loss of the toe-pinch reflex, each mouse was placed on a small animal physiological monitoring device connected to a head-fixation frame (Harvard Apparatus). The cisterna magna (CM) was revealed by making an incision and reflecting the muscles overlying the back of the skull, as previously described.[28] CM injection was then performed using a 30-gauge dental needle (SOPIRA® Carpule®) connected to a 100 µl Hamilton syringe (Hamilton) via polyethylene (PE) 10 tubing (AgnTho's). The cannula was fixed to the skull using glue and dental cement. Alexa Fluor™ 647 conjugated bovine serum albumin [BSA-647, 67 kDa, 10 mg/ml, diluted in artificial CSF (aCSF), A34785, Invitrogen] was injected into the CM at a rate of 1 µl/min for a total volume of 10 µl using a KDS Legato 100 single infusion syringe pump (KD Scientific).

CSF tracer imaging and quantifications

At the experimental end points, *in vivo* transcranial images of each mouse were captured using a Nikon SMZ25 stereomicroscope with a Plan Apo 0.5× objective [numerical aperture (NA) 0.08] and an Andor Zyla VSC-04095 camera. After imaging, the mice were decapitated, and their brains were rapidly extracted and fixed overnight in 4% paraformaldehyde by immersion. Following fixation, *ex vivo* brain images were acquired using the same SMZ25 microscope. Mean tracer intensity within defined regions of interest was quantified using ImageJ software (v.1.53c).

Brains were then sectioned into 100-μm-thick coronal slices using a Leica V1200S vibratome (Leica Biosystems). For tracer analysis in brain sections, five slices per mouse, spanning from bregma +2 to −2 mm, were imaged with a Nikon ECLIPSE Ti2 microscope using a Plan Apo 4× λ objective (NA 0.2) and a Nikon DS-Qi2 camera. Following automated slice artefact removal, mean tracer intensity across each whole brain slice masked by a common threshold was calculated using Python (v.3.11.5). All analysis codes are openly available online: https://github.com/kswanberg/Osv/blob/main/20240419_Image_Processing_Methods.pdf.

Intracerebroventricular injection and intraparenchymal injection

Mice were anaesthetized with isoflurane (2.5%–3.5% in O_2 for induction, 1.5%–2.5% in O_2 for maintenance, 0.8–1 l/min flow rate) and positioned in a stereotactic frame. The body temperature was maintained using a heating pad. After exposing the dorsal skull, a burr hole was drilled at the designated coordinates. A glass capillary connected to a Hamilton syringe (Hamilton Company) was inserted slowly into the target brain structure. After injection, the capillary was left in place for 5 min to minimize backflow before being slowly withdrawn. The incision was subsequently closed using Histoacryl® surgical glue (B. Braun Medical AB), and bupivacaine (Marcain® 5 mg/ml, Aspen Nordics) was applied subcutaneously for local analgesia. Mice were allowed to recover in a heated cage until fully awake.

For intracerebroventricular injection of Aβ, the lateral ventricle was targeted at anteroposterior −0.2 mm; mediolateral −1.0 mm; dorsoventral −2.0 mm from the dura. A total volume of 6 μl aCSF or $Aβ_{1–42}$-HiLyte™ Fluor 647 (AS64161, Anaspec) or non-fluorescent $Aβ_{1–42}$ (AS20276, Anaspec) was injected at 1 μl/min. The $Aβ_{1–42}$ peptide was reconstituted using 1.0% NH_4OH in aCSF as the solvent following the manufacturer's instructions and was prepared as a 0.5 μg/μl working solution.

For intracerebroventricular injection of liposome to deplete brain macrophages, the lateral ventricle was targeted at anteroposterior −0.2 mm; mediolateral −1.0 mm; dorsoventral −2.0 mm from the dura. A mannosylated macrophage depletion kit (m-Clodrosome® + m-Encapsome®, SKU# CLD-8914, Encapsula) was used. A total volume of 8 μl of m-Clodrosome or m-Encapsome (control liposome) was injected at a rate of 1 μl/min.

For intraparenchymal tracer injections, the striatum was targeted at anteroposterior +0.6 mm; mediolateral −2.0 mm; dorsoventral −3.3 mm from the skull. A total of 1 μl of fluorescent tracer mixture was injected at a rate of 0.2 μl/min. The fluorescent tracer mixture contained Alexa Fluor™ 647-conjugated 67 kDa BSA (3.3 mg/ml in aCSF) and Texas Red™-conjugated 3 kDa dextran (D3328, Invitrogen; 3.3 mg/ml in aCSF). Forty-eight hours after injection, mice were anaesthetized with ketamine and xylazine and transcardially perfused with PBS and 4% paraformaldehyde. Brains were post-fixed by immersion in 4% paraformaldehyde overnight before further processing and analysis.

Brain clearing and light-sheet microscopy

To achieve optical clearing of the brains, a modified immunolabelling-enabled 3D imaging of solvent-cleared organs (iDISCO+) protocol was performed as previously described.[29,30] Briefly, samples were dehydrated in a graded series of methanol/H_2O solutions (20%, 40%, 60%, 80% and 100%; 1.5 h each) followed by another 100% methanol overnight. Delipidation was performed using methanol:dichloromethane (33%:66%) for 6 h, then washed twice with 100% dichloromethane (30 min each). Samples were subsequently immersed in ethyl cinnamate (ECi, 100%) for ≥7 days before imaging. Cleared brains were imaged using a LaVision UltraMicroscope Blaze light-sheet microscope (Miltenyi Biotec) controlled by ImSpectorPro software (Miltenyi Biotec). Imaging was performed with a 1.1× objective (Miltenyi Biotec MI PLAN 1.1×, numerical aperture 0.1) and 6 μm step size. Filter sets used included: excitation at 488 nm with emission at 525/50 nm for structure reference; excitation at 640 nm with emission at 680/30 nm for injected BSA-647 imaging, and excitation at 561 nm with emission at 595/40 nm for injected 3 kDa Dextran-Texas Red™ imaging. The image stacks were imported into Arivis Vision4D v.3.5 (Zeiss Arivis) for 3D reconstruction and analysis. 3D reconstructed brains were analysed using the built-in Analysis Pipeline of Arivis Vision4D. The sum intensity and sum volume of all voxels with an intensity value above a constant threshold were calculated to assess glymphatic clearance from the brain as previously described.[31]

Immunohistochemistry, imaging and quantifications

Immunostaining was performed on 100-μm thick brain sections. Briefly, sections were first blocked for 3 h at room temperature (RT) under gentle shaking in a blocking solution containing 1% BSA, 5% normal donkey serum, 0.5% Triton X-100 and 0.5% Tween-20 in PBS. After blocking, sections were incubated with primary antibodies overnight at 4°C under gentle shaking. Following primary antibody incubation, sections were washed, then incubated with appropriate secondary antibodies (1:500) for 2 h at RT under gentle shaking. Before final mounting, slices were counterstained with 4′,6-diamidino-2-phenylindole (DAPI) (1:1000, D1306, Invitrogen).

The primary antibodies used in this study included: rabbit-anti-Lyve1 (1:300, PA5-19620, Invitrogen), rabbit-anti-Laminin (1:1500, L9393, Merck), rat-anti-CD206 (1:300, MCA2235, Bio-Rad), rabbit-anti-AQP4 (1:250, AB3594, Millipore), rabbit-anti-$Aβ_{1–42}$ (H31L21) (1:750, 700254, Invitrogen) and rabbit-anti-$Aβ_{1–40}$ (1:500, IBL #18580). The secondary antibodies used in this study included: donkey-anti-rabbit Alexa Fluor® 568 (A10042, Invitrogen), donkey-anti-rat Alexa Fluor® 568 (ab175475, Abcam), donkey-anti-rabbit Alexa Fluor® 488 (A21206, Invitrogen) and donkey-anti-rat Alexa Fluor® 488 (10123952, Invitrogen).

For staining with rabbit-anti-$Aβ_{1–42}$ (H31L21) and rabbit-anti-$Aβ_{1–40}$, slices were incubated in 85% formic acid at RT for 10 min before blocking. For staining with rabbit anti-laminin, slices were incubated with pepsin (R2283, Merck) at 37°C for 10–15 min before blocking. Lectin staining (*Lycopersicon esculentum*, 1:200, L0401, Sigma-Aldrich) was performed together with DAPI staining by incubating slices for 20 min at RT under gentle shaking.

Confocal images were acquired using a Nikon A1RHD confocal scanning microscope with a Plan Apo 20× λ objective (N.A. 0.75) and a Nikon A1plus camera. Image analysis and quantification were performed using ImageJ software (v.1.53c). Confocal images of the leptomeninges covering the dorsal cortex were acquired for quantification of leptomeningeal macrophages. For quantification of PVMs, all macrophages along vessels within the defined regions of interest were included, regardless of vessel diameter. AQP4 polarization along cerebral blood vessels was quantified as previously described.[31,32] Briefly, blood vessels were selected randomly from confocal images and analysed cross-sectionally using the line plot tool in ImageJ. The line was drawn to include both the AQP4 signal

at the vascular endfeet and the surrounding parenchymal region. The AQP4 polarization index was calculated as the ratio of the average peak fluorescence intensity at the vascular endfeet to the average intensity in the adjacent parenchyma.

Flow cytometry

Mice were anaesthetized with intraperitoneal ketamine and xylazine and transcardially perfused with PBS before brain collection. Brain tissue suspensions were prepared using the Neural Tissue Dissociation Kit (130-092-628, Miltenyi Biotec) according to the manufacturer's protocol. $CD11b^+$ cells, containing brain macrophages, were enriched by magnetic-activated cell sorting (MACS) using CD11b microbeads (130-093-634, Miltenyi Biotec). Fc receptor blocking was performed before staining using anti-mouse CD16/32 (1:100, 156604, BioLegend). Cells were analysed using a FACS Aria™ III cytometer (BD Biosciences) with FACS Diva software (BD Biosciences). Viable cells were identified using propidium iodide (PI) staining (1:1000, 421301, BioLegend), and PI-negative cells were gated for further analysis. Antibodies used included: anti-mouse CD38-PE-vio770 (1:50, 130-102-374, Miltenyi Biotec), anti-mouse MHCII-PE (1:50, 130-102-186, Miltenyi Biotec), anti-mouse CD206-PerCP-eFluor™ 710 (1:100, 46-2061-82, Invitrogen) and anti-mouse CD45-APC-Vio® 770 (1:100, 130-118-559, Invitrogen). CD38 was used as a substitute for Lyve1 in flow cytometry according to a previous study.[33] Data were analysed with FlowJo software v.10.4.0 (Becton Dickinson and Company).

For *in vitro* phagocytosis assays, $CD11b^+$ cells, including brain macrophages, were incubated with $A\beta_{1–42}$-HiLyte™ Fluor 647 (AS64161, Anaspec, 2.5 μM) and 1.0 μm FluoSpheres™ Polystyrene Microspheres (505/515 nm yellow–green fluorescent, F13081, Invitrogen, ~200 microspheres/cell) at 37°C for 30 min in a cell incubator. After incubation, the cells were thoroughly washed and stained with appropriate antibodies before analysis with a FACS Aria™ III cytometer.

Anti-Aβ treatment

Male and female homozygous 20-week-old App^{NL-F} mice were used in this experiment. The recombinant antibodies RmAb158[34,35] (targeting aggregated Aβ) and RmAbSynO2[36,37] (targeting aggregated alpha-synuclein, used as a control IgG) were generated as previously described. Antibody (10 mg/kg) was administered intraperitoneally in PBS solution once a week for 5 weeks consecutively. Seven days after the final dose, end-point experiments were conducted on the mice.

CSF collection and Multiplex CSF Aβ electrochemiluminescence immunoassay

Mice were anaesthetized with intraperitoneal ketamine and xylazine. After loss of the toe-pinch reflex, each mouse was placed on a small animal physiological monitoring device connected to a head fixation frame (Harvard Apparatus). The CM was exposed as previously described. A 30-gauge dental needle (SOPIRA® Carpule®) was then inserted into the CM. The needle was connected to a 1 ml syringe via PE-50 tubing (AgnTho's). CSF was collected by gently pulling back on the syringe plunger. Aβ concentrations in CSF were quantified using the Mesoscale Discovery (MSD) platform with the MSD V-PLEX 6E10 Kit ($A\beta_{1–38}$, $A\beta_{1–40}$ and $A\beta_{1–42}$; K1200E-2), following the manufacturer's instructions. Plates were read with a QuickPlex Q120 instrument, and data were analysed using MSD Discovery Workbench software.

Y-maze task

Spontaneous alternation behaviour in the Y-maze was used to assess spatial working memory performance, as previously described.[38] Briefly, mice were placed in one arm of a Y-shaped maze, where the three arms (30 cm length × 15 cm height × 5 cm width) were arranged at 120° angles from each other. Mice were allowed to explore the maze freely for 8 min, while being recorded by a camera placed above the maze. The videos were analysed using ANY-maze (Stoelting Europe). A spontaneous alternation was defined as consecutive entries into all three different arms without repetition. The percentage of spontaneous alternation was calculated as 100 × (number of alternations) / (total number of arm entries − 2), providing a measure of spatial working memory performance.

Statistical analysis

All statistical analyses were conducted using GraphPad Prism v.10 (GraphPad Software). Data normality was assessed using the Shapiro–Wilk test and the D'Agostino–Pearson omnibus (K^2) test. The specific statistical tests used for each dataset, along with the corresponding sample size (n), are detailed in the respective figure legends. Statistical significance was determined using Student's unpaired two-tailed t-test, the Mann–Whitney U-test (for non-normal distributions) or Welch's t-test (for unequal variances) when comparing two independent groups, and paired t-test when comparing values from the same group. For comparisons involving three independent groups, one-way ANOVA, Brown–Forsythe ANOVA (for unequal variances) or the Kruskal–Wallis test (for non-normal distributions) was used, followed by appropriate multiple-comparisons tests. For comparisons involving two factors, two-way ANOVA or repeated-measures two-way ANOVA was applied, with appropriate multiple-comparisons tests. For the two-way ANOVA, datasets that did not meet the assumption of normality were $\log_2$--transformed prior to statistical testing to satisfy the requirements of parametric analysis. For correlation analyses, Pearson's correlation ($n \geq 20$ and parametric) or Spearman's correlation ($n < 20$ or non-parametric) was used. A P-value of <0.05 was considered statistically significant for rejecting the null hypothesis.

Results

Glymphatic impairment occurs in App^{NL-F} mice, but not in rapid Aβ-plaque-accumulating App^{NL-G-F} mice

App^{NL-G-F} mice exhibited apparent Aβ plaque deposition as early as 2 months of age (Supplementary Fig. 1A, F and G) and displayed significant spatial memory deficit at 12 months (Supplementary Fig. 2), consistent with previous findings.[22] To assess glymphatic influx function in these mice, CM injection with the fluorescent tracer BSA-647 was performed at 2, 4 and 12 months of age and compared with age-matched WT mice (Supplementary Fig. 1A). Surprisingly, despite rapid Aβ deposition, glymphatic influx in these mice remained comparable to age-matched WT controls at all examined ages, based on both *in vivo* and *ex vivo* CSF tracer imaging quantification (Supplementary Fig. 1B–E). Furthermore, no correlation was observed between glymphatic influx and parenchymal $A\beta_{1–42}$ burden of App^{NL-G-F} mice at any age (Supplementary Fig. 1H–J) or overall (Supplementary Fig. 1K).

Unlike App^{NL-G-F} mice, App^{NL-F} mice exhibit a slower pattern of Aβ accumulation[22] and show only a minimal parenchymal $A\beta_{1–42}$ deposition at 6 months of age (Fig. 1A, I and J). Interestingly, a significant decrease in glymphatic influx was found in App^{NL-F} mice

at 6 months of age compared with WT mice, as shown by both *in vivo* and *ex vivo* CSF tracer imaging (Fig. 1B–E), which was confirmed by brain slice quantification (Fig. 1F–H). Again, no correlation was observed between glymphatic influx and $A\beta_{1–42}$ burden across ages (Fig. 1K), supporting that glymphatic impairment occurs independently of parenchymal Aβ deposition in *App* knock-in models.

Two-way ANOVA also showed a significant main effect of age, confirming an age-dependent decline in glymphatic influx, as reported previously.[39] However, the interaction between age and genotype was not significant, indicating that the magnitude of age-related decline did not differ between genotypes.

We also assessed $A\beta_{1–40}$ expression in the mice. $A\beta_{1–40}$ levels were much lower and were detectable only in 12-month-old App^{NL-G-F} mice. No correlation was found between glymphatic influx and parenchymal $A\beta_{1–40}$ level in this group (Supplementary Fig. 3).

To assess whether glymphatic clearance was impaired in App^{NL-F} mice, we performed intrastriatal injections of fluorescent tracer. The tracer was allowed to circulate and be cleared for 48 h before the mice were sacrificed. Residual tracer distribution throughout the brain 48 h post-injection was quantified and used as a measure of glymphatic clearance (Fig. 2A). Sum tracer volume and intensity around the injection site were significantly higher in App^{NL-F} mice than WT mice specifically at 6 months of age (Fig. 2B–G), suggesting impaired clearance of the injected tracer and reduced glymphatic clearance function.

Together, these data suggest that glymphatic dysfunction emerges selectively in App^{NL-F} mice at 6 months of age, a stage at which parenchymal Aβ plaque deposition is still minimal.

Impairment of glymphatic influx in App^{NL-F} mice is correlated with loss of PBMs

It is well established that polarization of AQP4 water channels to the astrocytic endfeet is crucial for efficient glymphatic function.[9] To investigate whether impaired AQP4 polarization contributes to glymphatic dysfunction in App^{NL-F} mice, we calculated their AQP4 polarization index. Our analysis revealed no significant difference in AQP4 polarization between App^{NL-F} mice and WT mice at 4, 6 and 12 months of age (Supplementary Fig. 4), suggesting that the reduced glymphatic influx observed in App^{NL-F} mice at 6 months is not attributable to disrupted AQP4 polarization and that other mechanisms might be responsible for this effect.

It was reported recently that PBMs regulate CSF flow and glymphatic influx by affecting vascular pulsatility.[14] Our own data also confirmed that depletion of PBMs using clodronate liposome led to a reduced glymphatic influx (Supplementary Fig. 5). We next investigated whether PBM populations are altered in App^{NL-F} mice. Using CD206 immunostaining on brain sections, there was a significant reduction in both leptomeningeal and perivascular macrophage populations in App^{NL-F} mice at 6 months of age, compared with age-matched WT mice (Fig. 3A–E). Correlation analysis confirmed that the number of perivascular macrophages was positively correlated with glymphatic influx at 6 months of age (Fig. 3F–H). In contrast, the number of PBMs was preserved in the App^{NL-G-F} mice (Supplementary Fig. 1L–N).

Acute injection of Aβ into the CSF impairs brain PBMs and leads to impairment of glymphatic influx

Both human and animal studies have shown that increased parenchymal Aβ deposition is associated with reduced levels of Aβ in the CSF.[40,41] Thus, Alzheimer's disease models with slow and late-onset parenchymal Aβ plaque formation, such as App^{NL-F} mice, have a prolonged period of elevated CSF Aβ levels. Meanwhile, in mouse models with rapid Aβ plaque accumulation, such as the App^{NL-G-F} mouse model, the period with high levels of Aβ in the CSF is shorter. Correspondingly, our data confirmed that the level of $A\beta_{1–42}$ in the CSF was significantly higher in App^{NL-F} mice than App^{NL-G-F} mice (Supplementary Fig. 6A–C). We thus next investigated whether Aβ in the CSF was sufficient to trigger a loss of PBMs.

To test this, $A\beta_{1–42}$ was introduced into the CSF of C57BL/6 mice via lateral ventricular injection (Fig. 4A). The dynamic changes of CSF concentration of $A\beta_{1–42}$ after injection were validated by multiplex electrochemiluminescence immunoassay (Supplementary Fig. 7A). The peak concentration at 3 h after injection in our experiment was consistent with a previous study reporting a similar concentration at 30 min after injection.[42] Similar concentrations were observed in 7-month-old App^{NL-F} mice in our experiments (Supplementary Fig. 6A) and in cognitively unimpaired humans (~500–1500 pg/ml), as previously reported.[43-45] Flow cytometry revealed a significant reduction in the number of PBMs at 24 h, but not 3 h after $A\beta_{1–42}$ injection (Fig. 4B and C). Further analysis of PBM subtypes indicated that the most notable decrease occurred in $CD38^+$ macrophages (i.e. the $Lyve1^+$ macrophages) (Fig. 4D). After intracerebroventricular injection of $A\beta_{1–42}$, brain macrophages were found to phagocytose the injected $A\beta_{1–42}$ (Fig. 4E–G and Supplementary Fig. 7B). Subtype analysis confirmed that $CD38^+$ macrophages were the primary population responsible for $A\beta_{1–42}$ uptake (Fig. 4E). These findings suggest that the reduction in macrophage numbers mainly affected the subset engaged in $A\beta_{1–42}$ phagocytosis. Moreover, macrophages were capable of degrading the phagocytosed $A\beta_{1–42}$, as evidenced by a decrease in both the percentage of $A\beta_{1–42}^+$ macrophages and the median $A\beta_{1–42}$ signal intensity from 3 to 24 h post-injection (Fig. 4F and G). Additional analysis showed that $MHCII^+$ macrophages were more efficient at degrading $A\beta_{1–42}$, as indicated by lower levels of residual $A\beta_{1–42}$ in these cells 24 h after the injection (Fig. 4H).

We next asked whether these acute Aβ-induced changes in PBMs were associated with impairment of glymphatic influx. We found that $A\beta_{1–42}$-injected mice showed significantly reduced glymphatic influx and fewer PBMs in comparison to controls (Fig. 5A–H). Moreover, the abundance of PBMs was positively correlated with glymphatic influx efficiency (Fig. 5I–K).

Together, the data suggest that a high level of Aβ in the CSF is toxic to PBMs and that this is associated with subsequent glymphatic dysfunction.

Enhanced Aβ phagocytosis in brain macrophages of App^{NL-G-F} but not App^{NL-F} mice

Brain macrophages are professional phagocytes. Aβ phagocytosis and clearance are considered protective responses against the progression of Alzheimer's disease.[46,47] We next assessed the phagocytic function of macrophages from App^{NL-F} mice using *in vitro* phagocytosis assays with fluorescently labelled $A\beta_{1–42}$ and microspheres (Fig. 6A). Flow cytometry analysis revealed that the phagocytic capacity for engulfing microspheres was similar among macrophages from App^{NL-G-F}, App^{NL-F} and age-matched WT mice (Fig. 6B and C). However, macrophages from App^{NL-G-F} mice exhibited augmented phagocytosis of $A\beta_{1–42}$, which was accompanied by upregulated MHCII expression (Fig. 6D–F). Macrophages from App^{NL-F} mice failed to upregulate their Aβ-specific phagocytic capacity, in contrast to the App^{NL-G-F} model, indicating specificity in this compensatory response.

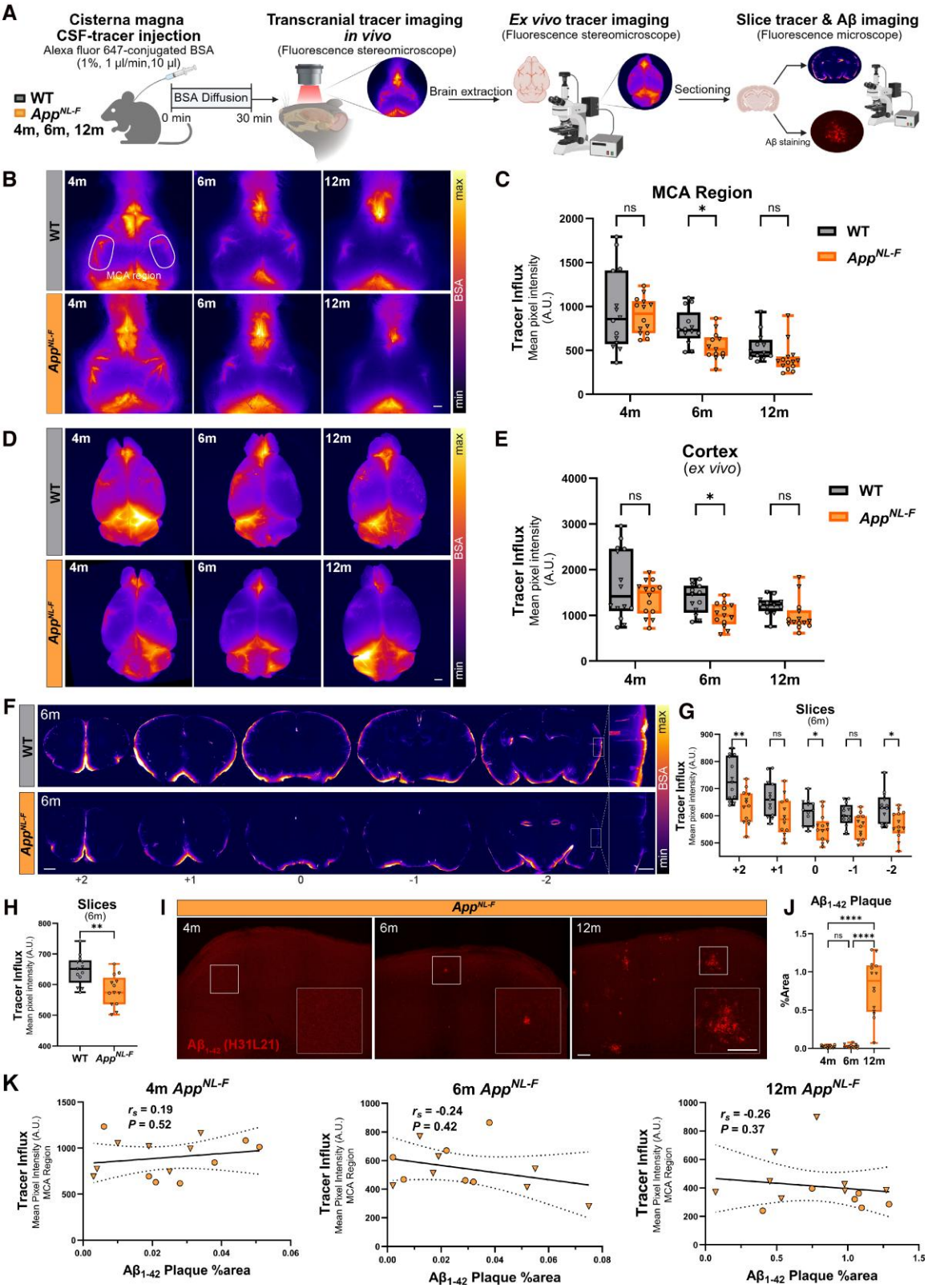

Figure 1 ***App*$^{NL-F}$ mice exhibit reduced glymphatic influx into the brain prior to significant parenchymal Aβ plaque deposition.** (**A**) Schematic representation of experimental design. Created with BioRender.com. Liu, N. (2026) https://BioRender.com/6n2eis1. (**B**) Representative images of CSF tracer distribution *in vivo* at the dorsal skull 30 min after injection. Scale bar = 1000 µm. (**C**) Quantification of mean fluorescence intensity of CSF tracer influx (*in vivo*) at the MCA region 30 min after injection. Statistical tests were performed after $\log_2$ transformation of the original data, two-way ANOVA with Šídák's multiple comparisons, $n = 12–14$. (**D**) Representative images of CSF tracer distribution *ex vivo* at the dorsal surface. Scale bar = 1000 µm. (**E**) Quantification of mean fluorescence intensity of CSF tracer influx (*ex vivo*) at the dorsal cortex (two-way ANOVA with Šídák's multiple comparisons, $n = 12–14$). (**F**) Representative images of CSF tracer distribution (*ex vivo*) in coronal brain slices (−2, −1, 0, +1 and +2 mm from bregma).

(Continued)

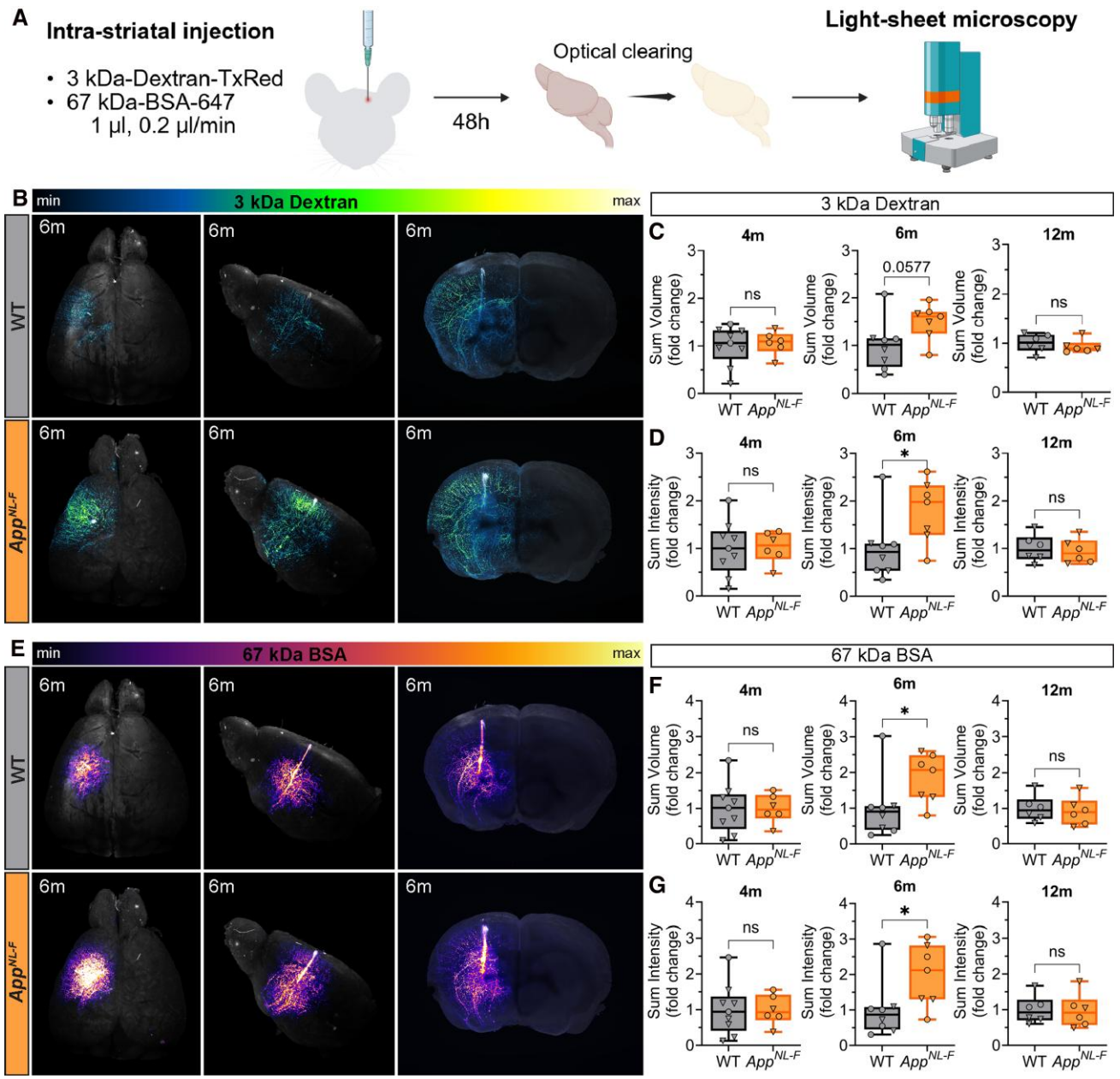

Figure 2 Decreased glymphatic clearance in 6-month-old *App*$^{NL-F}$ mice. (**A**) Schematic representation of experimental design. Created with BioRender.com. Liu, N. (2026) https://BioRender.com/r7h0i0t. (**B**) Representative 3D reconstructed images of optically cleared brains showing the distribution of injected fluorescent 3 kDa dextran: dorsal view (*left*), left lateral view (*middle*) and close-up anterior view (*right*). (**C**) Quantification of fold change in interstitial 3 kDa dextran sum volume remaining around the injection site (Student's unpaired two-tailed *t*-test or Mann–Whitney U-test, $n = 6–9$). (**D**) Quantification of fold change in interstitial 3 kDa dextran sum fluorescence intensity remaining around the injection site (Student's unpaired two-tailed *t*-test or Mann–Whitney U-test, $n = 6–9$). (**E**) Representative 3D reconstructed images of optically cleared brains showing the distribution of injected fluorescent 67 kDa BSA: dorsal view (*left*), left lateral view (*middle*) and close-up anterior view (*right*). (**F**) Quantification of fold change in interstitial 67 kDa BSA sum volume remaining around the injection site (Student's unpaired two-tailed *t*-test or Mann–Whitney U-test, $n = 6–9$). (**G**) Quantification of fold change in interstitial 67 kDa BSA sum fluorescence intensity remaining around the injection site (Student's unpaired two-tailed *t*-test or Mann–Whitney U-test, $n = 6–9$). Box plots show the median, interquartile range and full data range. Each point represents data from one animal; circles denote female mice, and triangles denote male mice. $^{*}P < 0.05$; ns = not significant. BSA = bovine serum albumin; m = month; WT = wild-type.

Figure 1 Continued

Scale bar = 1000 µm; 250 µm in *inset*. (**G**) Quantification of mean fluorescence intensity of CSF tracer influx in coronal brain slices by location (−2, −1, 0, +1 and +2 mm from bregma) (repeated measures two-way ANOVA with Šídák's multiple comparisons test, $n = 13, 13$). (**H**) Quantification of CSF tracer influx in coronal brain slices averaged across all five brain slices collected (Student's unpaired two-tailed *t*-test, $n = 13, 13$). (**I**) Representative confocal images of $A\beta_{1–42}$ staining in the dorsal cortex. Scale bar = 100 µm. (**J**) Quantification of percentage area of $A\beta_{1–42}$ plaque in dorsal cortex (Brown–Forsythe ANOVA test with Dunnett's T3 multiple comparisons test, $n = 13–14$). (**K**) Spearman correlation analysis between CSF tracer influx and $A\beta_{1–42}$ deposition level at different ages. Box plots show median, interquartile range and full data range. Each point represents data from one animal; circles denote female mice, and triangles denote male mice. $^{*}P < 0.05$, $^{**}P < 0.01$ and $^{****}P < 0.0001$; ns = not significant. BSA = bovine serum albumin; MCA = middle cerebral artery; m = month; r_s = non-parametric Spearman correlation coefficient; WT = wild-type.

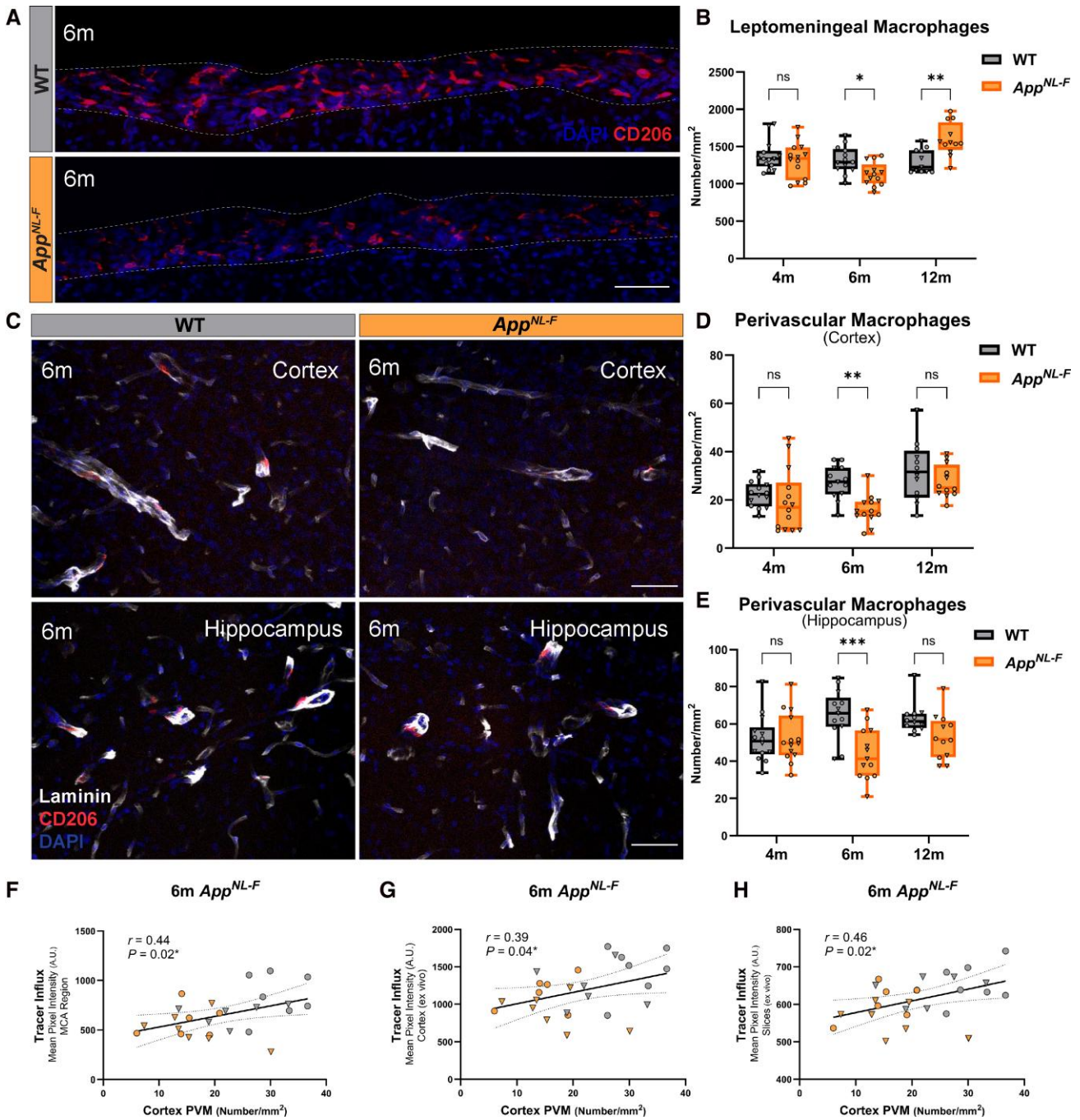

Figure 3 Glymphatic influx impairment in *App*$^{NL-F}$ mice is correlated with loss of parenchymal border macrophages. (**A**) Representative images of CD206$^+$ leptomeningeal macrophages in 6-month-old *App*$^{NL-F}$ and WT mice. Scale bar = 50 μm. (**B**) Quantification of the number of CD206$^+$ leptomeningeal macrophages in each group (two-way ANOVA with Šídák's multiple comparisons, $n = 11$–14). (**C**) Representative images of CD206$^+$ PVM in cortex and hippocampus of *App*$^{NL-F}$ and WT mice at 6 months old. Scale bar = 50 μm. (**D**) Quantification of the number of cortical CD206$^+$ PVMs in each group (two-way ANOVA with Šídák's multiple comparisons, $n = 12$–14). (**E**) Quantification of the number of hippocampal CD206$^+$ PVMs in each group (two-way ANOVA with Šídák's multiple comparisons, $n = 12$–14). (**F**–**H**) Pearson correlation analysis between CSF tracer influx and the number of cortical CD206$^+$ PVMs at 6 months old. ($n = 25$–26). Box plots show the median, interquartile range and full data range. Each point represents data from one animal; circles denote female mice, and triangles denote male mice. *$P < 0.05$, **$P < 0.01$ and ***$P < 0.001$; ns = not significant. BSA = bovine serum albumin; m = month; MCA = middle cerebral artery; PVM = perivascular macrophage; r = Pearson correlation coefficient; WT = wild-type.

Anti-Aβ treatment increases leptomeningeal macrophages in *App*$^{NL-F}$ mice but not glymphatic influx

Recent clinical trials have demonstrated promising effects of anti-Aβ immunotherapy in slowing cognitive decline in patients with Alzheimer's disease.[4,48] To investigate whether PBMs contribute to this therapeutic effect by modulating the glymphatic system, we treated *App*$^{NL-F}$ mice systemically with the recombinant murine version of anti-Aβ antibody lecanemab (RmAb158) for 5 weeks, starting at 4 months of age, prior to the onset of parenchymal Aβ deposition (Fig. 7A). This anti-Aβ antibody treatment significantly

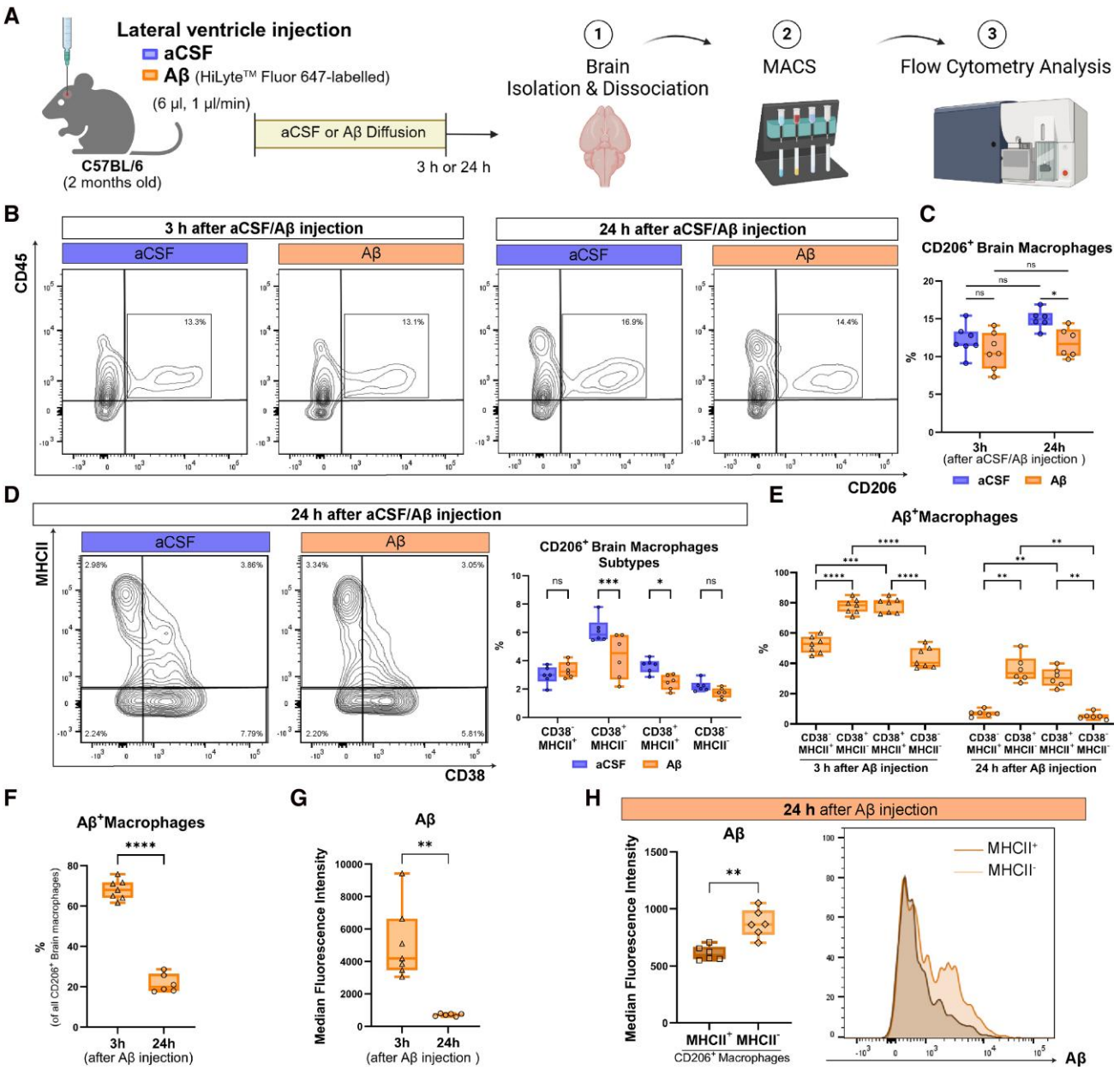

Figure 4 Acute Aβ injection into the CSF impairs brain macrophages. (**A**) Schematic representation of experimental design. Created with BioRender.com. Liu, N. (2026) https://BioRender.com/e1a2ppp. (**B**) Representative flow cytometry plots of CD45$^+$CD206$^+$ macrophages in each group from live cells. (**C**) The percentage of CD206$^+$ macrophages in the total CD11b$^+$ live cell population in each group (two-way ANOVA with Šídák's multiple comparisons, $n = 6$–7). (**D**) Representative flow cytometry plots of CD206$^+$ macrophages subtypes in each group and quantification of the percentages of CD206$^+$ macrophage subtypes in the total CD11b$^+$ live cell population in each group (two-way ANOVA with Šídák's multiple comparisons, $n = 6$, 6). (**E**) The percentage of Aβ$^+$ macrophages in each CD45$^+$CD206$^+$ macrophages subtype population (repeated-measures two-way ANOVA with Šídák's multiple comparisons, $n = 6$–7). (**F**) The percentage of Aβ$^+$ macrophages in the total CD45$^+$CD206$^+$ macrophage population in each group (Student's unpaired two-tailed *t*-test, $n = 6$, 7). (**G**) The median fluorescence intensity of Aβ of CD45$^+$CD206$^+$ macrophages in each group (Student's unpaired two-tailed *t*-test, $n = 6$, 7). (**H**) Quantification and histogram plot of the median fluorescence intensity of Aβ in MHCII$^+$ or MHCII$^-$ macrophages (Student's paired two-tailed *t*-test, $n = 6$). Box plots show the median, interquartile range and full data range. Each point represents data from one animal. *P < 0.05, **P < 0.01, ***P < 0.001 and ****P < 0.0001; ns = not significant. aCSF = artificial CSF; MACS = magnetic-activated cell sorting.

reduced parenchymal Aβ deposition (Fig. 7G and H). However, it failed to restore glymphatic function in *App*$^{NL-F}$ mice (Fig. 7B–F). Correlation analysis confirmed that glymphatic influx function was independent of parenchymal Aβ$_{1–42}$ burden (Fig. 7I). Consistent with human trials,[48,49] reduced parenchymal Aβ levels were accompanied by a trend towards an increased concentration of Aβ in the CSF (Supplementary Fig. 6D–F) after anti-Aβ immunotherapy. Notably, the treatment restored leptomeningeal macrophage numbers (Fig. 7J–L). However, the PVM population was not rescued; instead, their numbers were further reduced in the hippocampus (Fig. 7M–R). These findings suggest that although anti-Aβ therapy can restore leptomeningeal macrophages, it is insufficient to reverse glymphatic dysfunction, probably owing to persistent and exacerbated deficits in the PVM population.

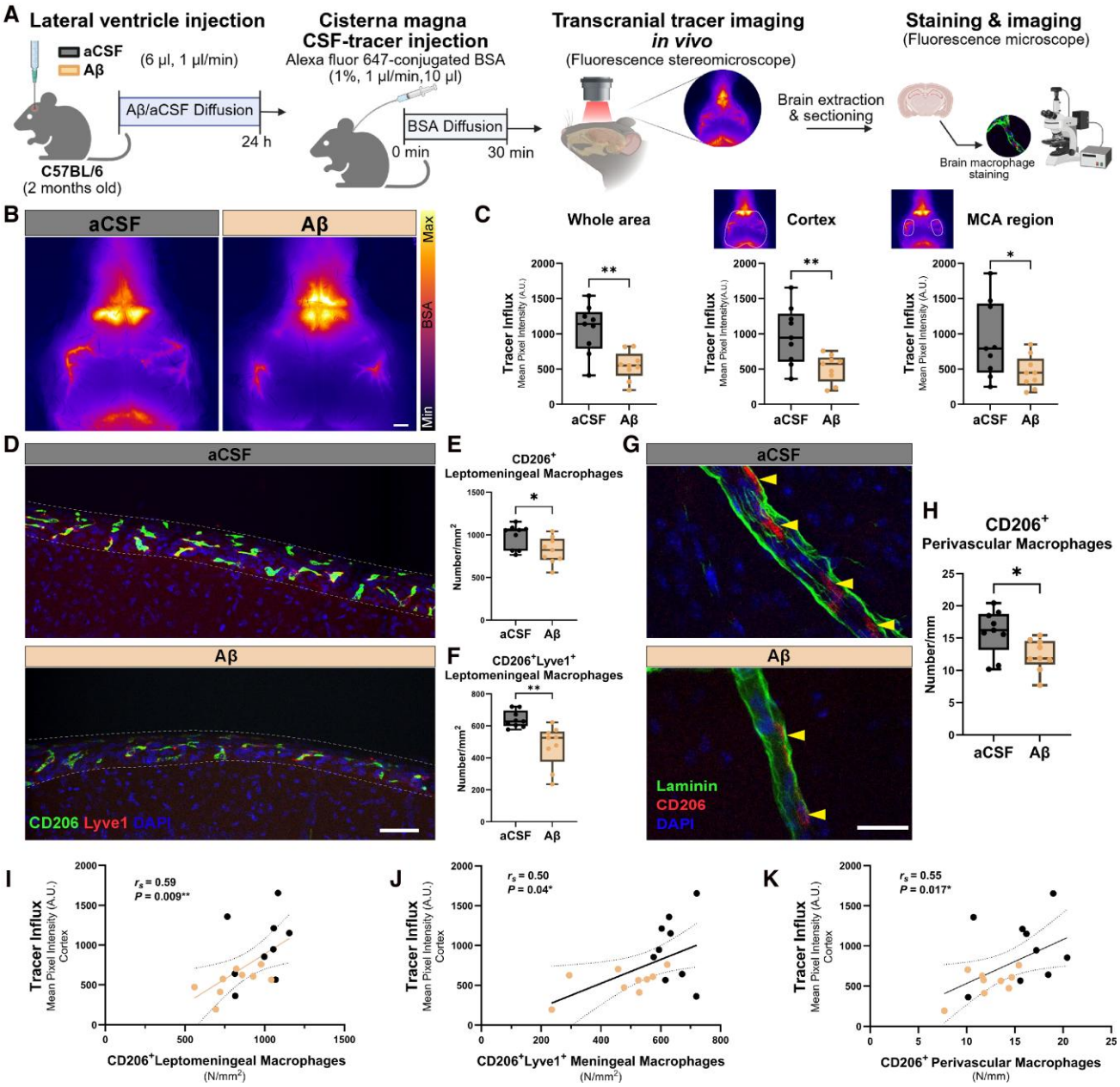

Figure 5 Acute Aβ injection into the CSF reduces glymphatic influx and is associated with loss of parenchymal border macrophages. (**A**) Schematic representation of experimental design. Created with BioRender.com. Liu, N. (2026) https://BioRender.com/axqm6tt. (**B**) Representative *in vivo* images of CSF tracer distribution at the dorsal skull 30 min after injection. Scale bar = 1000 µm. (**C**) Quantification of mean fluorescence intensity of CSF tracer influx (*in vivo*) at different brain regions (Student's unpaired two-tailed *t*-test or unpaired *t*-test with Welch's correction, $n = 9, 9$). (**D**) Representative images of $CD206^+Lyve1^+$ leptomeningeal macrophages in each group. Scale bar = 50 µm. (**E**) Quantification of the number of $CD206^+$ leptomeningeal macrophages in each group (Student's unpaired two-tailed *t*-test, $n = 9, 9$). (**F**) Quantification of the number of $CD206^+Lyve1^+$ leptomeningeal macrophages in each group (Student's unpaired *t*-test with Welch's correction, $n = 9, 9$). (**G**) Representative images of $CD206^+$ perivascular macrophages in the cortex of each group. Scale bar = 25 µm. (**H**) Quantification of the number of $CD206^+$ perivascular macrophages in each group (Student's unpaired two-tailed *t*-test, $n = 9, 9$). (**I–K**) Spearman correlation analysis between CSF tracer influx and number of brain macrophages ($n = 18$). Box plots show the median, interquartile range and full data range. Each point represents data from one animal. $^*P < 0.05$ and $^{**}P < 0.01$. aCSF = artificial CSF; BSA = bovine serum albumin; MCA = middle cerebral artery; r_s = non-parametric Spearman correlation coefficient.

Discussion

This study revealed that glymphatic impairment during the progression of Alzheimer's disease is not correlated with parenchymal Aβ burden or AQP4 polarization but is instead associated with the loss of PBMs. Acute exposure to $A\beta_{1–42}$ in the CSF impaired brain macrophages and decreased glymphatic influx, supporting a direct role for CSF Aβ toxicity.

In this study, we observed impaired glymphatic function in App^{NL-F} mice, but not in App^{NL-G-F} mice. App^{NL-G-F} mice, carrying the additional Arctic mutation, exhibit accelerated Aβ aggregation and subsequent pathology, with plaque deposition beginning as early as 2 months.

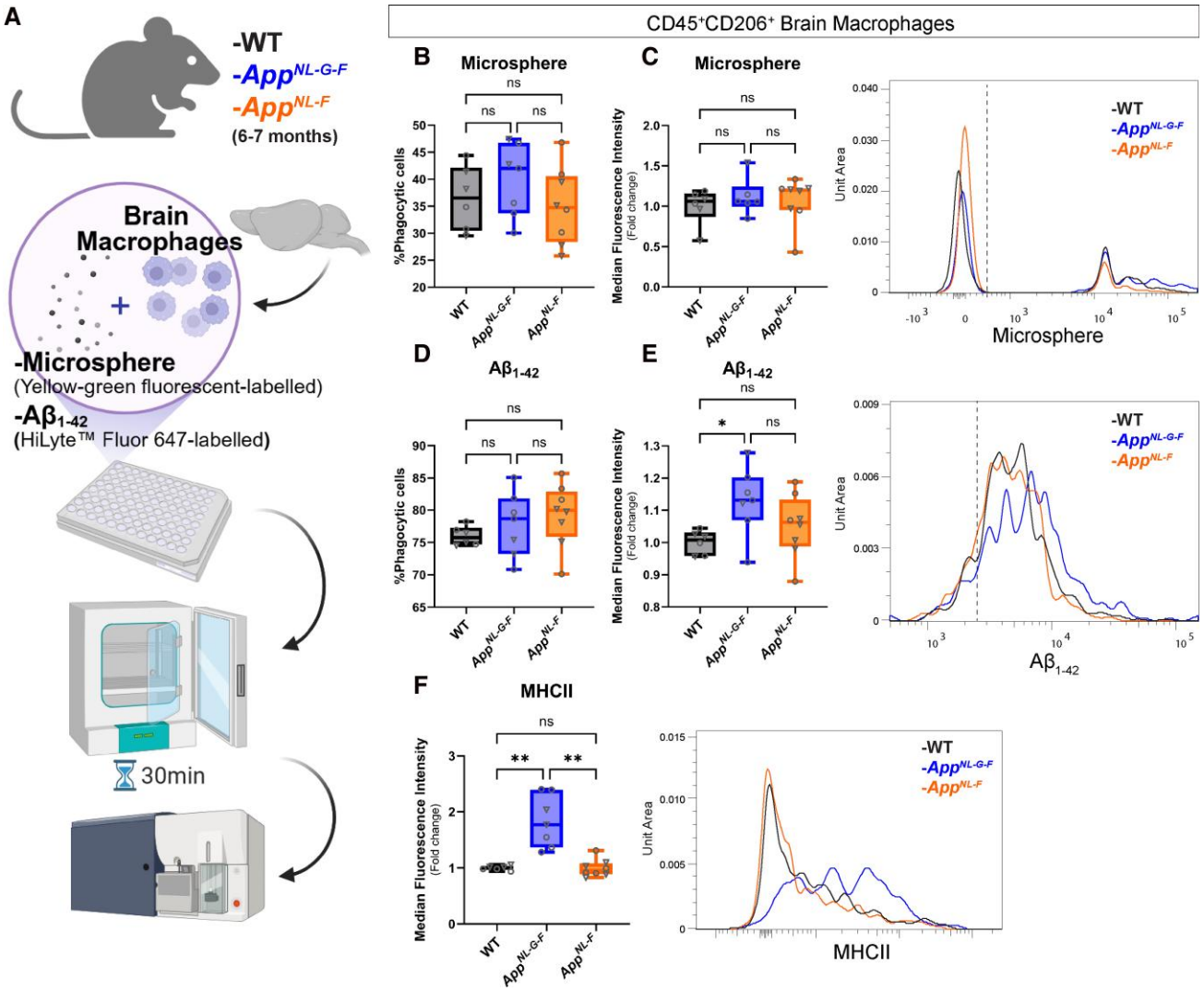

Figure 6 Enhanced Aβ phagocytosis in brain macrophages of *App*$^{NL\text{-}G\text{-}F}$ but not *App*$^{NL\text{-}F}$ mice. (**A**) Schematic representation of experimental design. Created with BioRender.com. Liu, N. (2026) https://BioRender.com/cqs1cbt. (**B**) The percentage of microsphere$^+$ macrophages in the total CD45$^+$CD206$^+$ macrophage population in each group (one-way ANOVA with Tukey's multiple comparisons test, $n = 6$–8). (**C**) Quantification and representative plot of the median fluorescence intensity of microsphere of CD45$^+$CD206$^+$ macrophages in each group (Kruskal–Wallis test with Dunn's multiple comparisons test, $n = 6$–8). (**D**) The percentage of Aβ$^+$ macrophages in the total CD45$^+$CD206$^+$ macrophage population in each group (Brown–Forsythe ANOVA test with Dunnett's T3 multiple comparisons test, $n = 6$–8). (**E**) Quantification and representative plot of the median fluorescence intensity of Aβ of CD45$^+$CD206$^+$ macrophages in each group (one-way ANOVA with Tukey's multiple comparisons test, $n = 6$–8). (**F**) Quantification and representative plot of the median fluorescence intensity of MHCII in CD45$^+$CD206$^+$ macrophages in each group (Brown–Forsythe ANOVA test with Dunnett's T3 multiple comparisons test, $n = 6$–8) and representative histogram plots of each group. Box plots show the median, interquartile range and full data range. Each point represents data from one animal; circles denote female mice, and triangles denote male mice. $^*P < 0.05$ and $^{**}P < 0.01$; ns = not significant. m = month; WT = wild-type.

In contrast, *App*$^{NL\text{-}F}$ mice demonstrate a slower Aβ accumulation starting at ~6 months of age. This differential progression is mirrored by CSF Aβ dynamics, in that *App*$^{NL\text{-}G\text{-}F}$ mice show a sharp (>50%) decline in the Aβ level in the CSF between 1 and 6 months, whereas *App*$^{NL\text{-}F}$ mice exhibit only a modest reduction from 3 to 9 months.[50,51] Our study also confirms significantly higher CSF Aβ levels in *App*$^{NL\text{-}F}$ mice compared with *App*$^{NL\text{-}G\text{-}F}$ mice. We therefore propose the possibility that prolonged exposure to elevated CSF Aβ, rather than plaque burden, drives glymphatic dysfunction of *App*$^{NL\text{-}F}$ mice, at least in part via Aβ-driven toxicity in PBMs.

Glymphatic function has previously been studied in transgenic mouse models of Alzheimer's disease. In 2016, Peng *et al.*[17] first demonstrated impaired glymphatic influx in APPswe/PSEN1dE9 mice at both early (3–4 months) and later (12 months) stages of Aβ pathology. Similar findings were subsequently reported by other laboratories using the same model at 3 months,[15] 5 months[20,52] and 9 months of age.[20] Notably, APPswe/PSEN1dE9 mice typically begin to develop Aβ deposition at ~6 months of age, similar to the *App*$^{NL\text{-}F}$ mice.[53,54] In contrast, studies on 5xFAD mice, which exhibit early and rapid parenchymal Aβ deposition beginning as early as 1.5 months of age,[55] are limited and have yielded inconsistent results; one study reported increased CSF tracer influx in the prefrontal cortex at 5 months,[18] whereas another found decreased tracer influx across the brain at 4–5 months.[23] Collectively, these findings suggest that glymphatic impairment is observed more consistently in models with slower Aβ accumulation, supporting our hypothesis that prolonged CSF Aβ elevation, rather than parenchymal Aβ plaque

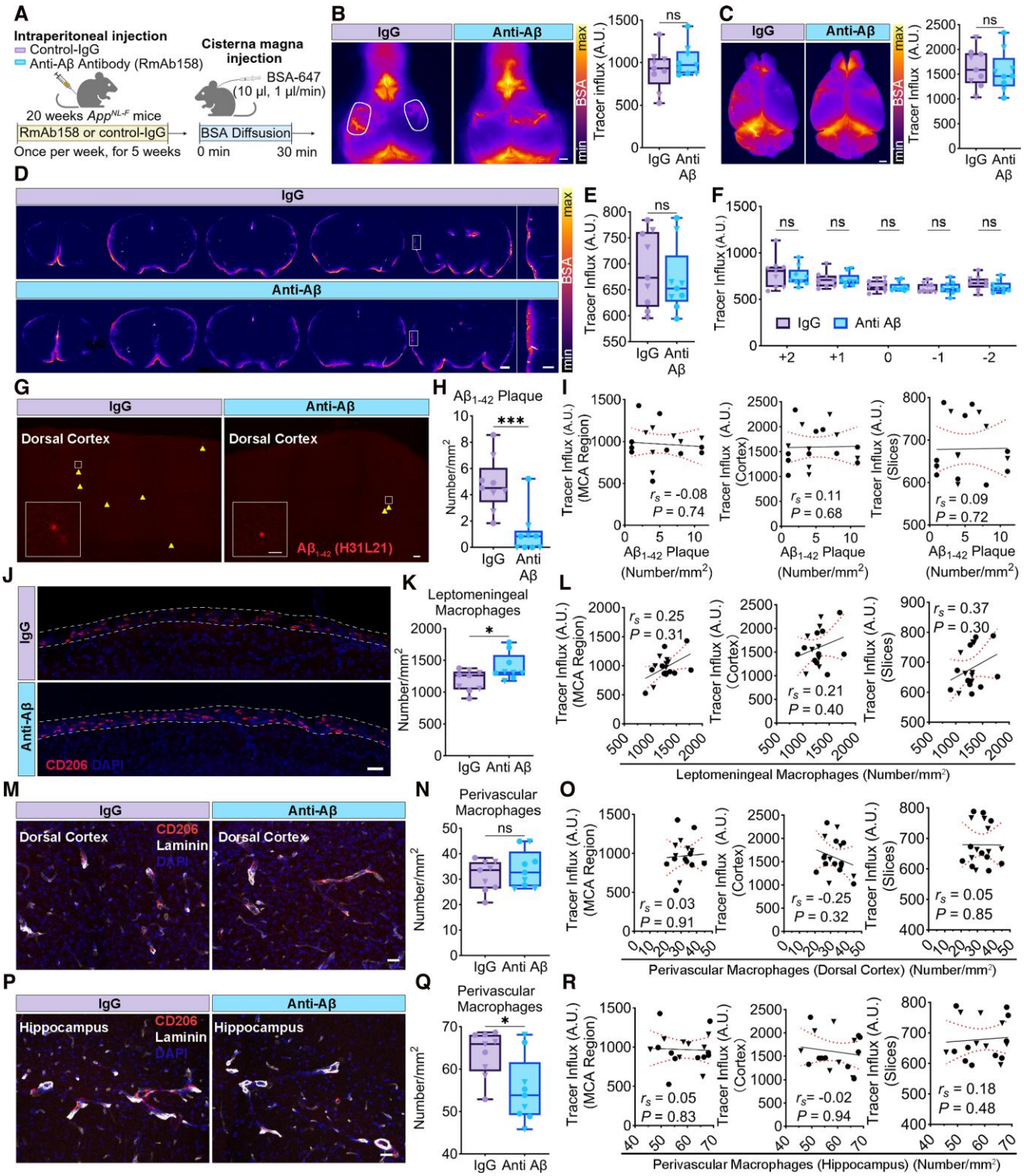

Figure 7 Anti-Aβ treatment increases leptomeningeal macrophages in App^{NL-F} mice but not glymphatic influx. (**A**) Schematic representation of experimental design. Created with BioRender.com. Liu, N. (2026) https://BioRender.com/3jcl3eb. (**B**) Representative images and quantification of CSF tracer distribution (*in vivo*) of each group 30 min after injection. Scale bar = 1000 μm (Student's unpaired two-tailed *t*-test, $n = 9, 9$). (**C**) Representative images and quantification of CSF tracer distribution (*ex vivo*) of each group. Scale bar = 1000 μm (Student's unpaired two-tailed *t*-test, $n = 9, 9$). (**D**) Representative images of CSF tracer distribution (*ex vivo*) in coronal brain slices. Scale bar = : 1000 μm. (**E**) Quantification of CSF tracer influx in coronal brain slices averaged across all five brain slices collected (Student's unpaired two-tailed *t*-test, $n = 9, 9$). (**F**) Quantification of mean fluorescence intensity of CSF tracer influx in coronal brain slices by location (−2, −1, 0, +1 and +2 mm from bregma) (repeated-measures two-way ANOVA with Šídák's multiple comparisons, $n = 9, 9$). (**G**) Representative confocal images of $A\beta_{1–42}$ staining in the dorsal cortex. Scale bar = 100 μm; 25 μm in *inset*. (**H**) Quantification of $A\beta_{1–42}$ plaque in dorsal cortex (Student's unpaired two-tailed *t*-test, $n = 9, 9$). (**I**) Spearman correlation analysis between CSF tracer influx and $A\beta_{1–42}$ deposition level. $n = 18$. (**J**) Representative images of $CD206^+$ leptomeningeal macrophages in each group. Scale bar = 25 μm. (**K**) Quantification of

(Continued)

load, plays a more crucial role in driving glymphatic dysfunction during the progression of Alzheimer's disease.

Another important factor to consider when revisiting the glymphatic findings from transgenic APP models is that these models can exhibit glymphatic alterations driven not only by Aβ pathology but also by APP-derived metabolites. Transgenic APP models often involve non-physiological overexpression of mutant APP, leading to excess production not only of Aβ but also of various APP-derived fragments. Several studies have shown that non-Aβ APP fragments can affect AQP4 polarization, suggesting a potential mechanistic link between APP overexpression and glymphatic dysfunction. For instance, secreted amyloid precursor protein alpha (sAPPα) has been shown to downregulate dystrophin in astrocytes, a key regulator of AQP4 polarization.[56,57] Overexpression of β-site amyloid precursor protein cleaving enzyme 1 (BACE1) has also been reported to reduce AQP4 polarization in mice.[58] Additionally, APP/PS1 mice with locomotor hyperactivity, a phenotype that has been linked to changes in APP metabolism,[59] exhibit pronounced AQP4 depolarization compared with normally active counterparts.[59,60] In contrast, the *App*$^{NL\text{-}F}$ mice in our study retained normal AQP4 polarization, supporting the possibility that glymphatic dysfunction found in APP-overexpression models might be influenced by APP-derived metabolites that affect astrocytic function.

As professional phagocytic immune cells, PBMs play a key role in surveying the brain borders for exogenous and endogenous antigens, including Aβ.[24] Previous studies have demonstrated the toxic effects of Aβ on macrophages both *in vitro* and *in vivo*, particularly in relationship to apoptotic pathways.[61,62] Our data further confirmed that acute Aβ exposure leads to PBM loss, which is associated with subsequent glymphatic dysfunction. We therefore speculate that PBM loss in 6-month-old *App*$^{NL\text{-}F}$ mice might be attributed to the prolonged elevation of CSF Aβ levels in these mice. In contrast, brain macrophages remained intact in the *App*$^{NL\text{-}G\text{-}F}$ mice, a model with a rapid decrease in CSF Aβ. Surprisingly, PBM reduction in *App*$^{NL\text{-}F}$ mice did not persist as disease advanced. At 12 months, no decrease in PVMs was observed, and leptomeningeal macrophages even increased in comparison to age-matched controls. Notably, this rebound of PBMs coincided with the stabilization of its glymphatic function at this stage, despite continued parenchymal Aβ accumulation. This further supports our hypothesis that glymphatic dysfunction in *App* knock-in mice is not driven by parenchymal Aβ burden but rather more closely linked to macrophage abundance, which appears to be influenced greatly by CSF Aβ levels during the early stages of disease. Importantly, PBMs are long-lived, yolk sac-derived macrophages that are minimally replaced by bone marrow-derived cells,[63,64] even in Alzheimer's disease.[65] Thus, it would be particularly interesting for future studies to explore the mechanisms that promote PBM self-renewal at this later stage, when CSF Aβ levels are substantially lower. In addition, a recent study has shown that following pexidartinib (PLX3397)-induced depletion of brain macrophages, PBMs can be replaced by monocyte-derived cells. However, these replacements are transcriptionally distinct from their embryonically derived counterparts.[66,67] Therefore, it would also be valuable for future research to investigate whether the rebound of PBMs observed in 12-month-old *App*$^{NL\text{-}F}$ mice is functionally equivalent to the original population in roles beyond the regulation of glymphatic function.

In our study, we observed a trend towards increased CSF $A\beta_{1–42}$ levels following systemic anti-Aβ treatment in *App*$^{NL\text{-}F}$ mice, a phenomenon also reported in human anti-Aβ clinical trials.[48,49] These trials were conducted in symptomatic patients with confirmed amyloid positivity, in whom post-treatment increases in CSF $A\beta_{1–42}$ have been associated with improved cognitive outcomes.[68] In contrast, our intervention was performed at a presymptomatic stage, when *App*$^{NL\text{-}F}$ mice exhibit minimal parenchymal plaque deposition but relatively high baseline CSF $A\beta_{1–42}$ levels. In our study, the biological effects of anti-Aβ treatment appear complex. On the one hand, anti-Aβ-treated mice exhibited slower accumulation of parenchymal plaques, suggesting effective limitation of Aβ aggregation. On the other hand, the treatment induced region-specific effects on PBMs. We observed a further reduction in hippocampal PVM density, supporting the notion that elevated CSF $A\beta_{1–42}$ levels after treatment might impose additional challenges on PBMs. However, PVM density in the cortex was not affected, and leptomeningeal macrophages exhibited the opposite trend. The increase in leptomeningeal macrophages is in line with a previous report showing elevated numbers of brain macrophages 3 days after intracranial anti-Aβ antibody administration.[69] However, how anti-Aβ immunotherapy might specifically stimulate macrophage renewal in the leptomeningeal compartment, despite the elevated CSF $A\beta_{1–42}$ levels observed in our study, remains unclear. An alternative explanation is that elevated CSF Aβ levels might promote the migration of brain macrophages towards the leptomeningeal compartment. Supporting this hypothesis, a previous gene ontology analysis identified significant enrichment of pathways related to macrophage migration following anti-Aβ immunotherapy.[70] Nonetheless, the precise mechanisms underlying these regional effects remain to be elucidated. Overall, the treatment failed to rescue glymphatic dysfunction in *App*$^{NL\text{-}F}$ mice. The inability to restore the PVM population might partly account for this outcome. Alternatively, a longer treatment duration might be required to achieve glymphatic recovery. Further studies are needed to elucidate the mechanisms underlying these region-specific effects, which might ultimately help to optimize anti-Aβ therapeutic strategies.

Our findings might have important clinical implications. Although CSF Aβ levels are known to decline in patients with symptomatic Alzheimer's disease,[40] growing evidence also suggests a biphasic pattern, with an initial increase in CSF Aβ levels at the early stages of the disease. Elevated CSF Aβ levels have been reported in

Figure 7 Continued
the number of CD206$^+$ leptomeningeal macrophages in each group (Student's unpaired two-tailed *t*-test, $n = 9, 9$). (**L**) Spearman correlation analysis between CSF tracer influx and the number of CD206$^+$ leptomeningeal macrophages, $n = 18$. (**M**) Representative images of CD206$^+$ perivascular macrophages in the cortex of each group. Scale bar = 25 μm. (**N**) Quantification of the number of CD206$^+$ perivascular macrophages in the cortex of each group (Student's unpaired two-tailed *t*-test, $n = 9, 9$). (**O**) Spearman correlation analysis between CSF tracer influx and the number of cortical CD206$^+$ perivascular macrophages, $n = 18$. (**P**) Representative images of CD206$^+$ perivascular macrophages in the hippocampus of each group. Scale bar = 25 μm. (**Q**) Quantification of the number of CD206$^+$ perivascular macrophages in the hippocampus of each group (Student's unpaired two-tailed *t*-test, $n = 9, 9$). (**R**) Spearman correlation analysis between CSF tracer influx and the number of hippocampal CD206$^+$ perivascular macrophages, $n = 18$. Box plots show the median, interquartile range and full data range. Each point represents data from one animal; circles denote female mice, and triangles denote male mice. *$P < 0.05$ and *** $P < 0.001$. aCSF = artificial CSF; BSA = bovine serum albumin; MCA = middle cerebral artery; r_s = non-parametric Spearman correlation coefficient.

several transgenic mouse models, including APP23,[71] APP24,[71] APP51,[71] APP/PS1[72] and 3xTg AD mice,[73] prior to the onset of parenchymal plaque deposition. In humans, an early increase in CSF Aβ levels has been observed during the preclinical phase, from younger (<50 years) to older (<60 years) individuals.[74] Another cohort study demonstrated that Aβ level in the CSF in ApoE4-negative individuals was predicted to rise between 25 and 50 years of age.[75] Additionally, increased CSF Aβ levels have been detected in young adults carrying autosomal dominant familial Alzheimer's disease mutations more than two decades before the onset of clinical symptoms.[76] Although larger longitudinal cohort studies including younger participants are needed to confirm these findings, current evidence supports the existence of an initial period of an elevated level of Aβ in the CSF, which might represent a critical window of vulnerability for brain macrophages during development of Alzheimer's disease. Failure or loss of brain macrophages during this window could subsequently induce glymphatic dysfunction and accelerate Aβ-associated progression, forming a vicious cycle. Moreover, other conditions, such as sleep disturbance or deprivation and traumatic brain injury,[77-80] have also been reported to elevate CSF Aβ levels, thereby imposing additional Aβ-related stress on brain macrophages.

Conclusion

In summary, our study highlights that glymphatic impairment in *App* knock-in models is not directly correlated with parenchymal Aβ burden but is instead closely associated with the number of PBMs, which appears highly influenced by CSF Aβ dynamics during the early stages of disease. These findings suggest that therapeutic strategies aimed at preserving or enhancing brain macrophage function, particularly during the early stages, might offer additional opportunities to prevent or delay glymphatic dysfunction and the progression of Alzheimer's disease.

Data availability

The data that supports the findings of this study are available from the corresponding author, upon reasonable request.

Acknowledgements

The *App* knock-in mice were initially kindly provided by Takaomi Saido and Takashi Saito at RIKEN Center for Brain Science. We thank Anastasiia Kolomiiets and Jari Jukkola from Iben Lundgaard's laboratory for their helpful technical input and support during the early stages of this work. The thumbnail image for the online table of contents was created with BioRender.com. Liu, N. (2026) https://BioRender.com/ugenm39.

Funding

This study was funded by the private initiative: Innovative ways to fight Alzheimer's disease—Leif Lundblad Family and others to I.L. and P.N. The study was also funded by the Olle Engkvist Foundation and the Swedish Research Council (VR) to I.L.

Competing interests

The authors report no competing interests.

Supplementary material

Supplementary material is available at Brain online.

References

1. Scheltens P, de Strooper B, Kivipelto M, et al. Alzheimer's disease. *Lancet*. 2021;397:1577-1590.
2. Tahami Monfared AA, Byrnes MJ, White LA, Zhang Q. Alzheimer's disease: Epidemiology and clinical progression. *Neurol Ther*. 2022;11:553-569.
3. Rajan KB, Weuve J, Barnes LL, McAninch EA, Wilson RS, Evans DA. Population estimate of people with clinical Alzheimer's disease and mild cognitive impairment in the United States (2020–2060). *Alzheimers Dement*. 2021;17:1966-1975.
4. Jucker M, Walker LC. Alzheimer's disease: From immunotherapy to immunoprevention. *Cell*. 2023;186:4260-4270.
5. Plog BA, Nedergaard M. The glymphatic system in central nervous system health and disease: Past, present, and future. *Annu Rev Pathol*. 2018;13:379-394.
6. Hussain R, Graham U, Elder A, Nedergaard M. Air pollution, glymphatic impairment, and Alzheimer's disease. *Trends Neurosci*. 2023;46:901-911.
7. Ringstad G, Valnes LM, Dale AM, et al. Brain-wide glymphatic enhancement and clearance in humans assessed with MRI. *JCI Insight*. 2018;3:e121537.
8. Iliff JJ, Wang M, Liao Y, et al. A paravascular pathway facilitates CSF flow through the brain parenchyma and the clearance of interstitial solutes, including amyloid β. *Sci Transl Med*. 2012;4:147ra111.
9. Mestre H, Hablitz LM, Xavier AL, et al. Aquaporin-4-dependent glymphatic solute transport in the rodent brain. *Elife*. 2018;7:e40070.
10. Gomolka RS, Hablitz LM, Mestre H, et al. Loss of aquaporin-4 results in glymphatic system dysfunction via brain-wide interstitial fluid stagnation. *Elife*. 2023;12:e82232.
11. Venero JL, Vizuete ML, Machado A, Cano J. Aquaporins in the central nervous system. *Prog Neurobiol*. 2001;63:321-336.
12. Zeppenfeld DM, Simon M, Haswell JD, et al. Association of perivascular localization of aquaporin-4 with cognition and Alzheimer disease in aging brains. *JAMA Neurol*. 2017;74:91-99.
13. Simon M, Wang MX, Ismail O, et al. Loss of perivascular aquaporin-4 localization impairs glymphatic exchange and promotes amyloid β plaque formation in mice. *Alzheimers Res Ther*. 2022;14:59.
14. Drieu A, Du S, Storck SE, et al. Parenchymal border macrophages regulate the flow dynamics of the cerebrospinal fluid. *Nature*. 2022;611:585-593.
15. Feng W, Zhang Y, Wang Z, et al. Microglia prevent beta-amyloid plaque formation in the early stage of an Alzheimer's disease mouse model with suppression of glymphatic clearance. *Alzheimers Res Ther*. 2020;12:125.
16. Xu Z, Xiao N, Chen Y, et al. Deletion of aquaporin-4 in APP/PS1 mice exacerbates brain Aβ accumulation and memory deficits. *Mol Neurodegener*. 2015;10:58.
17. Peng W, Achariyar TM, Li B, et al. Suppression of glymphatic fluid transport in a mouse model of Alzheimer's disease. *Neurobiol Dis*. 2016;93:215-225.
18. Lin Y, Jin J, Lv R, et al. Repetitive transcranial magnetic stimulation increases the brain's drainage efficiency in a mouse model of Alzheimer's disease. *Acta Neuropathol Commun*. 2021;9:102.
19. Koundal S, Chen X, Gursky Z, et al. Divergent brain solute clearance in rat models of cerebral amyloid angiopathy and Alzheimer's disease. *iScience*. 2024;27:111463.

20. Liu Y, Hu P-P, Zhai S, et al. Aquaporin 4 deficiency eliminates the beneficial effects of voluntary exercise in a mouse model of Alzheimer's disease. *Neural Regen Res*. 2022;17:2079-2088.
21. Saito T, Matsuba Y, Yamazaki N, Hashimoto S, Saido TC. Calpain activation in Alzheimer's model mice is an artifact of APP and presenilin overexpression. *J Neurosci*. 2016;36:9933-9936.
22. Saito T, Matsuba Y, Mihira N, et al. Single *App* knock-in mouse models of Alzheimer's disease. *Nat Neurosci*. 2014;17:661-663.
23. Wu W, Zhao Y, Cheng X, et al. Modulation of glymphatic system by visual circuit activation alleviates memory impairment and apathy in a mouse model of Alzheimer's disease. *Nat Commun*. 2025;16:63.
24. Da Mesquita S, Rua R. Brain border-associated macrophages: Common denominators in infection, aging, and Alzheimer's disease? *Trends Immunol*. 2024;45:346-357.
25. Iliff JJ, Wang M, Zeppenfeld DM, et al. Cerebral arterial pulsation drives paravascular CSF–interstitial fluid exchange in the murine brain. *J Neurosci*. 2013;33:18190-18199.
26. Mestre H, Tithof J, Du T, et al. Flow of cerebrospinal fluid is driven by arterial pulsations and is reduced in hypertension. *Nat Commun*. 2018;9:4878.
27. Kiviniemi V, Wang X, Korhonen V, et al. Ultra-fast magnetic resonance encephalography of physiological brain activity – Glymphatic pulsation mechanisms? *J Cereb Blood Flow Metab*. 2016;36:1033-1045.
28. Xavier ALR, Hauglund NL, von Holstein-Rathlou S, et al. Cannula implantation into the cisterna magna of rodents. *J Vis Exp*. 2018(135):57378.
29. Renier N, Wu Z, Simon DJ, Yang J, Ariel P, Tessier-Lavigne M. iDISCO: A simple, rapid method to immunolabel large tissue samples for volume imaging. *Cell*. 2014;159:896-910.
30. Renier N, Adams EL, Kirst C, Wu Z, Azevedo R, Kohl J, et al. Mapping of brain activity by automated volume analysis of immediate early genes. *Cell*. 2016;165:1789–1802.
31. Kritsilis M, Vanherle L, Rosenholm M, et al. Loss of glymphatic homeostasis in heart failure. *Brain*. 2025;148:985-1000.
32. Pavan C, Xavier A LR, Ramos M, et al. DNase treatment prevents cerebrospinal fluid block in early experimental pneumococcal meningitis. *Ann Neurol*. 2021;90:653-669.
33. Mrdjen D, Pavlovic A, Hartmann FJ, et al. High-dimensional single-cell mapping of central nervous system immune cells reveals distinct myeloid subsets in health, aging, and disease. *Immunity*. 2018;48:380–395.e6.
34. Hultqvist G, Syvänen S, Fang XT, Lannfelt L, Sehlin D. Bivalent brain shuttle increases antibody uptake by monovalent binding to the transferrin receptor. *Theranostics*. 2017;7:308-318.
35. Gustavsson T, Metzendorf NG, Wik E, et al. Long-term effects of immunotherapy with a brain penetrating Aβ antibody in a mouse model of Alzheimer's disease. *Alzheimers Res Ther*. 2023;15:90.
36. Roshanbin S, Xiong M, Hultqvist G, et al. In vivo imaging of alpha-synuclein with antibody-based PET. *Neuropharmacology*. 2022;208:108985.
37. Roshanbin S, Julku U, Xiong M, et al. Reduction of αSYN pathology in a mouse model of PD using a brain-penetrating bispecific antibody. *Pharmaceutics*. 2022;14:1412.
38. Garcia-Serrano AM, Mohr AA, Philippe J, Skoug C, Spégel P, Duarte JMN. Cognitive impairment and metabolite profile alterations in the hippocampus and cortex of male and female mice exposed to a fat and sugar-rich diet are normalized by diet reversal. *Aging Dis*. 2022;13:267-283.
39. Kress BT, Iliff JJ, Xia M, et al. Impairment of paravascular clearance pathways in the aging brain. *Ann Neurol*. 2014;76:845-861.
40. Tapiola T, Alafuzoff I, Herukka S-K, et al. Cerebrospinal fluid β-amyloid 42 and tau proteins as biomarkers of Alzheimer-type pathologic changes in the brain. *Arch Neurol*. 2009;66:382-389.
41. Maia LF, Kaeser SA, Reichwald J, et al. Changes in amyloid-β and tau in the cerebrospinal fluid of transgenic mice overexpressing amyloid precursor protein. *Sci Transl Med*. 2013;5:194re2.
42. Cho SM, Kim HV, Lee S, et al. Correlations of amyloid-β concentrations between CSF and plasma in acute Alzheimer mouse model. *Sci Rep*. 2014;4:6777.
43. van Harten AC, Wiste HJ, Weigand SD, et al. Detection of Alzheimer's disease amyloid beta 1-42, p-tau, and t-tau assays. *Alzheimers Dement*. 2022;18:635-644.
44. Palmqvist S, Zetterberg H, Mattsson N, et al. Detailed comparison of amyloid PET and CSF biomarkers for identifying early Alzheimer disease. *Neurology*. 2015;85:1240-1249.
45. Rosenberg A, Öhlund-Wistbacka U, Hall A, et al. β-Amyloid, tau, neurodegeneration classification and eligibility for anti-amyloid treatment in a memory clinic population. *Neurology*. 2022;99:e2102-e2113.
46. Lai AY, McLaurin J. Clearance of amyloid-β peptides by microglia and macrophages: The issue of what, when and where. *Future Neurol*. 2012;7:165-176.
47. Rangaraju S, Raza SA, Li NXA, et al. Differential phagocytic properties of $CD45^{low}$ microglia and $CD45^{high}$ brain mononuclear phagocytes—Activation and age-related effects. *Front Immunol*. 2018;9:405.
48. van Dyck CH, Swanson CJ, Aisen P, et al. Lecanemab in early Alzheimer's disease. *N Engl J Med*. 2023;388:9-21.
49. Bittner T, Tonietto M, Klein G, et al. Biomarker treatment effects in two phase 3 trials of gantenerumab. *Alzheimers Dement*. 2025;21:e14414.
50. Andersson E, Lindblom N, Janelidze S, et al. Soluble cerebral Aβ protofibrils link Aβ plaque pathology to changes in CSF $Aβ_{42}$/$Aβ_{40}$ ratios, neurofilament light and tau in Alzheimer's disease model mice. *Nat Aging*. 2025;5:366-375.
51. Andersson E, Schultz N, Saito T, et al. Cerebral Aβ deposition precedes reduced cerebrospinal fluid and serum Aβ42/Aβ40 ratios in the $App^{NL\text{-}F/NL\text{-}F}$ knock-in mouse model of Alzheimer's disease. *Alzheimers Res Ther*. 2023;15:64.
52. Wang L, Zhang Y, Zhao Y, Marshall C, Wu T, Xiao M. Deep cervical lymph node ligation aggravates AD-like pathology of APP/PS1 mice. *Brain Pathol*. 2019;29:176-192.
53. Kamphuis W, Orre M, Kooijman L, Dahmen M, Hol EM. Differential cell proliferation in the cortex of the APPswePS1dE9 Alzheimer's disease mouse model. *Glia*. 2012;60:615-629.
54. Végh MJ, Heldring CM, Kamphuis W, et al. Reducing hippocampal extracellular matrix reverses early memory deficits in a mouse model of Alzheimer's disease. *Acta Neuropathol Commun*. 2014;2:76.
55. Oakley H, Cole SL, Logan S, et al. Intraneuronal β-amyloid aggregates, neurodegeneration, and neuron loss in transgenic mice with five familial Alzheimer's disease mutations: Potential factors in amyloid plaque formation. *J Neurosci*. 2006;26:10129-10140.
56. Peppercorn K, Kleffmann T, Hughes SM, Tate WP. Secreted amyloid precursor protein alpha (sAPPα) regulates the cellular proteome and secretome of mouse primary astrocytes. *Int J Mol Sci*. 2023;24:7165.
57. Amiry-Moghaddam M, Frydenlund DS, Ottersen OP. Anchoring of aquaporin-4 in brain: Molecular mechanisms and implications for the physiology and pathophysiology of water transport. *Neuroscience*. 2004;129:997–1008.
58. Zhou H, Gao F, Yang X, et al. Endothelial BACE1 impairs cerebral small vessels via tight junctions and eNOS. *Circ Res*. 2022;130:1321-1341.

59. Locci A, Orellana H, Rodriguez G, et al. Comparison of memory, affective behavior, and neuropathology in APP^{NLGF} knock-in mice to 5xFAD and APP/PS1 mice. *Behav Brain Res*. 2021;404:113192.
60. Wang T, Chen Y, Zou Y, et al. Locomotor hyperactivity in the early-stage Alzheimer's disease-like pathology of APP/PS1 mice: Associated with impaired polarization of astrocyte aquaporin 4. *Aging Dis*. 2022;13:1504-1522.
61. Zaghi J, Goldenson B, Inayathullah M, et al. Alzheimer disease macrophages shuttle amyloid-beta from neurons to vessels, contributing to amyloid angiopathy. *Acta Neuropathol*. 2009;117:111-124.
62. Caruso G, Benatti C, Musso N, et al. Carnosine protects macrophages against the toxicity of Aβ1-42 oligomers by decreasing oxidative stress. *Biomedicines*. 2021;9:477.
63. Goldmann T, Wieghofer P, Jordão MJC, et al. Origin, fate and dynamics of macrophages at central nervous system interfaces. *Nat Immunol*. 2016;17:797-805.
64. van Hove H, Martens L, Scheyltjens I, et al. A single-cell atlas of mouse brain macrophages reveals unique transcriptional identities shaped by ontogeny and tissue environment. *Nat Neurosci*. 2019;22:1021-1035.
65. Wu X, Saito T, Saido TC, Barron AM, Ruedl C. Microglia and $CD206^{+}$ border-associated mouse macrophages maintain their embryonic origin during Alzheimer's disease. *Elife*. 2021;10:e71879.
66. Vara-Pérez M, Movahedi K. Border-associated macrophages as gatekeepers of brain homeostasis and immunity. *Immunity*. 2025;58:1085-1100.
67. Bastos J, O'Brien C, Vara-Pérez M, et al. Monocytes can efficiently replace all brain macrophages and fetal liver monocytes can generate bona fide $SALL1^{+}$ microglia. *Immunity*. 2025;58:1269-1288.e12.
68. Abanto J, Dwivedi AK, Imbimbo BP, Espay AJ. Increases in amyloid-β_{42} slow cognitive and clinical decline in Alzheimer's disease trials. *Brain*. 2024;147:3513-3521.
69. Foley KE, Weekman EM, Krick KE, Johnson SN, Sudduth TL, Wilcock DM. Acute communication between microglia and nonparenchymal immune cells in the anti-Aβ antibody-injected cortex. *J Neurosci*. 2025;45:e1456242024.
70. Cadiz MP, Gibson KA, Todd KT, et al. Aducanumab anti-amyloid immunotherapy induces sustained microglial and immune alterations. *J Exp Med*. 2024;221:e20231363.
71. Maia LF, Kaeser SA, Reichwald J, et al. Increased CSF Aβ during the very early phase of cerebral Aβ deposition in mouse models. *EMBO Mol Med*. 2015;7:895-903.
72. Liu L, Herukka S-K, Minkeviciene R, van Groen T, Tanila H. Longitudinal observation on CSF Aβ42 levels in young to middle-aged amyloid precursor protein/presenilin-1 doubly transgenic mice. *Neurobiol Dis*. 2004;17:516-523.
73. Bjorkli C, Louet C, Flo TH, Hemler M, Sandvig A, Sandvig I. *In vivo* microdialysis in mice captures changes in Alzheimer's disease cerebrospinal fluid biomarkers consistent with developing pathology. *J Alzheimers Dis*. 2021;84:1781-1794.
74. Botella Lucena P, Vanherle S, Lodder C, et al. Blood-based Aβ42 increases in the earliest pre-pathological stage before decreasing with progressive amyloid pathology in preclinical models and human subjects: Opening new avenues for prevention. *Acta Neuropathol*. 2022;144:489-508.
75. Li G, Shofer JB, Petrie EC, et al. Cerebrospinal fluid biomarkers for Alzheimer's and vascular disease vary by age, gender, and *APOE* genotype in cognitively normal adults. *Alzheimers Res Ther*. 2017;9:48.
76. Reiman EM, Quiroz YT, Fleisher AS, et al. Brain imaging and fluid biomarker analysis in young adults at genetic risk for autosomal dominant Alzheimer's disease in the presenilin 1 E280A kindred: A case-control study. *Lancet Neurol*. 2012;11:1048-1056.
77. Emmerling MR, Morganti-Kossmann MC, Kossmann T, et al. Traumatic brain injury elevates the Alzheimer's amyloid peptide $A\beta_{42}$ in human CSF. A possible role for nerve cell injury. *Ann N Y Acad Sci*. 2000;903:118-122.
78. Varga AW, Wohlleber ME, Giménez S, et al. Reduced slow-wave sleep is associated with high cerebrospinal fluid Aβ42 levels in cognitively normal elderly. *Sleep*. 2016;39:2041-2048.
79. Liu H, Barthélemy NR, Ovod V, et al. Acute sleep loss decreases CSF-to-blood clearance of Alzheimer's disease biomarkers. *Alzheimers Dement*. 2023;19:3055-3064.
80. Blattner MS, Panigrahi SK, Toedebusch CD, et al. Increased cerebrospinal fluid amyloid-β during sleep deprivation in healthy middle-aged adults is not due to stress or circadian disruption. *J Alzheimers Dis*. 2020;75:471-482.